IEEE Access
Multidisciplinary ⋮ Rapid Review ⋮ Open Access Journal

Received 5 February 2024, accepted 18 March 2024, date of publication 22 March 2024, date of current version 1 April 2024.

Digital Object Identifier 10.1109/ACCESS.2024.3380838

RESEARCH ARTICLE

Broadband High-Efficiency Co-Polarized Wavefront Manipulation Based on Multi-Layered Metasurface for Terahertz Wave

SU ZONG[1] AND JIAJUN LIANG[2], (Senior Member, IEEE)
[1]College of Science and Technology, Gannan Normal University, Ganzhou, Jiangxi 341000, China
[2]Guangxi University Key Laboratory of Complex System Optimization and Big Data Processing, Yulin Normal University, Yulin, Guangxi 537000, China

Corresponding author: Jiajun Liang (shuigpjd@163.com)

This work was supported in part by Guangxi Natural Science Foundation under Grant 2021GXNSFBA220003.

ABSTRACT Metasurfaces can achieve multifunctional wavefront control, but most co-polarized metasurfaces can only achieve a 360° phase coverage at specific frequency points. In this paper, we propose a metasurface with efficient co-polarized Terahertz (THz) wave transmission and full 360° phase coverage over a wide band. The proposed metasurface consists of five metal layers and four dielectric layers, which can be equivalent to two cascade polarization converters to form a Fabry-Perot resonator. The forward incident *y*-polarized THz wave can transform into the same polarized transmission wave after transmitting the proposed metasurface. Electromagnetic waves interfere repeatedly inside the multilayer metasurface, resulting a high transmission efficiency; furthermore, by changing the structure parameters of the middle two metal layers, a full 360° phase coverage in the broadband is achieved. Wideband THz focus metalens, orbital angular momentum generator and holographic imaging are realized by properly arranging the metasurface unit cells. Simulation results show that the designed multifunctional metasurface can achieve good wavefront control over the band 0.7-1.0 THz. This paper provides a new idea for the design of broadband co-polarized metasurfaces, and has great potential value in communication, imaging, remote sensing and other fields.

INDEX TERMS Metasurface, co-polarized, wideband, wavefront control.

I. INTRODUCTION

With the popularization of 5G technology, spectrum resources are becoming scarce, and the development of Terahertz (THz) spectrum is an effective method to expand the communication frequency band. THz wave is located between microwave and infrared, which combines the excellent performance of electronics and photonics, and has many special characteristics [1], [2], [3]. However, most materials that exist in nature are difficult to generate effective response in THz frequency band, which leads to the research bottleneck and THz device research is still in initial stage at present [4]. The appearance of metasurface provides more options for designing THz devices. The common metasurface is composed of subwavelength artificial unit cells with the ability to regulate wave. It has special properties that natural materials do not have, such as negative refractive index, negative dielectric permittivity, negative magnetic conductivity and so on [5], [6], [7], and [8]. By arranging the artificial cell structure in a two-dimensional plane, discontinuous phase mutations can also be introduced to achieve arbitrary regulation of the electromagnetic wavefront. Nowadays, various THz devices based on the metasurface have been presented, such as THz metalens [9], [10], [11], [12], orbital angular momentum generator [13], [14], [15], THz absorber [16], [17], [18], etc.

The associate editor coordinating the review of this manuscript and approving it for publication was Roberta Palmeri.

At present, linear polarization wave phase control based on metasurface mainly by using the principle of phase transmission, which can realize wide band cross-polarization phase control and narrow band co-polarized phase control [19], [20], [21], [22], [23], [24]. By using the Fabry-Perot resonant principle, a metasurface with three-layer cell structure is proposed, which can achieve linear polarization conversion and 360° phase coverage in THz band, the polarization conversion efficiency can reach 60% [19]. Subsequently, a similar three-layer metasurface cell structure is presented, which can realize efficient linear polarization conversion and multifunctional wavefront control within the band 0.4-1.0 THz, and the polarization conversion efficiency can maintain more than 90% [20]. Such work provides a design method for designing a broadband THz wavefront manipulation, but this work is only based on cross-polarization conversion. In some specific cases, it is not expected to produce this polarization conversion, but requires a co-polarized transmission wave. The existing method is to change the size of the metal patch or to change the radius of the dielectric column in the full dielectric metasurface [25], [26]. A full-dielectric metasurface that can manipulate the phase of co-polarized in transmission and reflection modes is proposed, by changing the long and short axis of the elliptical column; but this structure can only achieve 360° phase coverage at a single frequency point [25]. At present, there are few reports on broadband co-polarized metasurface wavefront control. Therefore, it is meaningful to design a metasurface that can achieve 360° coverage of the co-polarized phase on a wide band, which can open the door to the co-polarized broadband wavefront control.

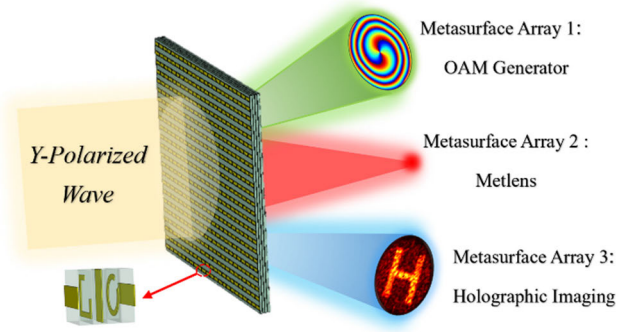

FIGURE 1. Schematic of the multifunctional metasurface.

Based on the principle of transmission phase, this paper proposes a multi-layer structure metasurface, which can realize arbitrary control of co-polarized wave phase at 0.7-1.0 THz band, and has high transmission efficiency. The proposed five-layer structure metasurface consists of a polarization-transition metasurface which is equivalent to two cascade polarization converters. The incident y polarization wave passes through the two polarization transformations and finally becomes a transmitted co-polarized wave. By changing the structure parameters of the middle two metal layers, arbitrary mutation phase can be realized at 0.7-1.0 THz. By using the proposed cell structure, a wideband metalens is also designed, which can achieve the focus effect within the band 0.7-1.0 THz. Then, a broadband orbital angular momentum generator and three high pattern purity vortex beams with pattern number $m = 1, 2, 3$ are generated. At last, we realized a wideband terahertz holographic imaging. The schematic of the multifunctional metasurface as shown in Figure 1. The proposed design provides new ideas for applications in photoelectric, communication, imaging and other fields etc.

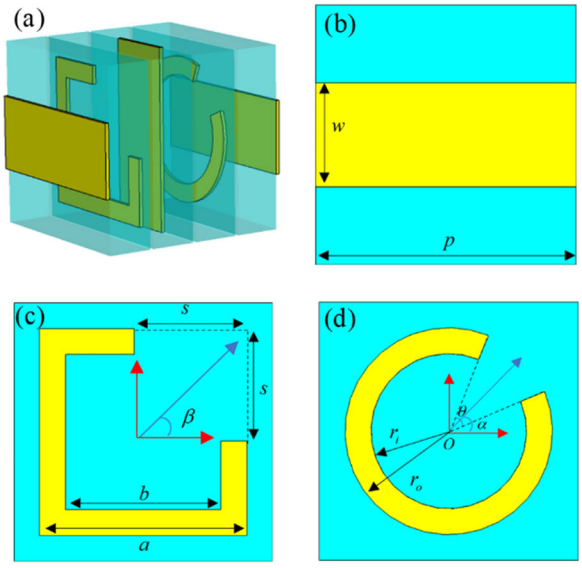

FIGURE 2. (a) 3D diagram of cell structure; (b) top layer of cell structure; (c) second layer of cell structure; (d) fourth layer of cell structure.

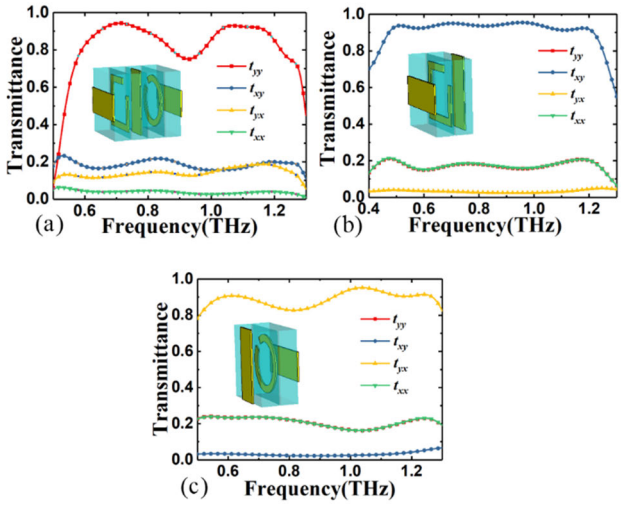

FIGURE 3. (a) Transmission coefficient of the five-layer cell structure; (b) transmission coefficient of structure A and (c) transmission coefficient of structure B.

II. UNIT CELL DESIGN AND ANALYSIS

The presented metasurface structure consists of five metal layers and four dielectric layers, as shown in Figure 2. The top

layer is a metal bar in the x direction, its width is w, as a grating, which can fully transmit the y-polarized electromagnetic wave, and completely reflected x-polarized electromagnetic wave; the third layer is also a metal bar with the orthogonal direction of the first layer, can completely through the x-polarized electromagnetic wave, and completely reflect the y-polarized electromagnetic wave; the fifth layer is a metal bar which is exactly the same as the top layer. The second layer of metasurface cell structure is a square opening ring, its outer diameter and inner diameter is a and b, respectively, the opening size is s, and the angle between the opening direction and the x axis is β. The fourth layer of metal is a circular opening ring, the outer diameter and inner diameter is r_o and r_i respectively, the opening angle size is θ, the angle of the opening ring center direction and the x-axis is α. In the simulation, the metal structure adopts copper with conductivity of $\sigma = 5.8 \times 10^7$ S/m, and thickness of 0.2 μm; the dielectric layer is a polyimide with thickness of 25 μm, its dielectric constant is 3.5, and the loss tangent is 0.0027. Through the optimization simulation, the optimal geometric parameters are: $p = 100$ um, $w = 40$ um, $a = 80$ um, $b = 60$ um, $r_o = 40$ um, $r_i = 30$ um. Broadband full 360° phase coverage can be achieved by changing the parameters s, β and θ.

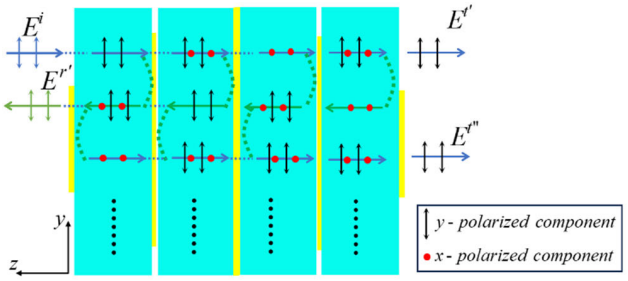

FIGURE 4. Schematic of the interference model.

The proposed five-layer cell structure can be decomposed into two types of three-layer polarization conversion cell structures, defined as structure A and B. Structure A can convert the incoming y-polarization wave along the forward direction to an x-polarization wave, while structure B can convert the incoming x-polarization wave into a y-polarization wave. By cascade structure A and B, the incident y polarization wave can be converted into a co-polarized transmission wave. As shown in Figure 3, the transmission coefficients of the proposed five-layer cell structure, structure A and B are given, respectively. In the five-layer cell structure simulation, we set the x and y-direction boundary condition to the periodic boundary and the z-direction to the open boundary. Figure 3 (a) shows the transmission coefficient of the proposed five-layer cell structure. It can be seen that the co-polarized transmission coefficient t_{yy} is greater than 0.7 in the band 0.6-1.2 THz and has a maximum value of 0.96 at 0.7 THz. At the same time, the co-polarized transmission coefficient t_{xx} and the cross-polarization transmission coefficient t_{xy} and t_{yx} are both suppressed below 0.2 in the working band. Figure 3 (b) shows the transmission coefficient of structure A. It can be seen that the cross-polarization coefficient t_{xy} is greater than 0.9 in the band 0.5-1.2 THz, showing a high polarization conversion performance. At the same time, the cross-polarization transmission coefficient t_{yx} and the co-polarized transmission coefficient t_{yy} and y_{xx} are both suppressed below 0.2 in the working band. Figure 3 (c) shows the transmission coefficient of structure B. Contrary to structure A, the cross-polarization coefficient t_{yx} is greater than 0.8 in the band 0.5-1.3 THz, and the incident x-polarization wave is almost completely converted into a y-polarization wave. The cross-polarization transmission coefficient t_{xy} and the co-polarized transmission coefficient t_{yy} and y_{xx} are both suppressed below 0.25 in the working frequency band. Through simulation analysis, structure A and structure B cascascade, the overall co-polarized transmission coefficient $t_{totalyy} = t_{Byx} \times t_{Axy}$.

To further analyze the physical mechanism of electromagnetic waves interference within the multilayer structure, an interference model is established. Figure 4 shows the interference process of electromagnetic waves in the five-layer structure metasurfaces. Where the black bidirectional arrow represents the y-polarized electromagnetic waves, while the red dot represents the x-polarized component. After the electromagnetic waves are incident to the top layer, it will be partially transmitted while the rest part is reflected. The electromagnetic waves are transmitted and reflected again after reaching the second layer. The electromagnetic waves reflected by the second layer are reflected again after reaching the first layer. Similarly, the electromagnetic waves reaching the third, fourth and fifth layers are also transmitted and reflected. Electromagnetic waves are transmitted and reflected several times in the five-layer structure, and the final total amount of transmission is the superposition of multiple transmission components. At the resonance frequency, the transmission efficiency can be effectively improved. The interference process is analyzed quantitatively.

Suppose we decompose the metasurface of the five-layer structure into separate five layers, and the transmission and reflection coefficient of each layer can be measured. We set the medium on both sides of an interface as α and β, and the electromagnetic waves transmitted on both sides can be connected with the 4×4 transmission matrix [19]:

$$\begin{pmatrix} E^f_{\beta x} \\ E^f_{\beta y} \\ E^b_{\beta x} \\ E^b_{\beta y} \end{pmatrix} = M_\delta \begin{pmatrix} E^f_{\alpha x} \\ E^f_{\alpha y} \\ E^b_{\alpha x} \\ E^b_{\alpha y} \end{pmatrix}. \tag{1}$$

where the subscripts x and y represent the electric field polarization state, the superscript f and b represent the forward and reverse propagation direction, respectively, and the

transmission matrix M_δ can be expressed as:

$$M_\delta = \begin{pmatrix} 1 & 0 & -\overleftarrow{r}_{xx}^{(\delta)} & -\overleftarrow{r}_{xy}^{(\delta)} \\ 0 & 1 & -\overleftarrow{r}_{yx}^{(\delta)} & -\overleftarrow{r}_{yy}^{(\delta)} \\ 0 & 0 & \overleftarrow{t}_{xx}^{(\delta)} & \overleftarrow{t}_{xy}^{(\delta)} \\ 0 & 0 & \overleftarrow{t}_{yx}^{(\delta)} & \overleftarrow{t}_{yy}^{(\delta)} \end{pmatrix}^{-1} \begin{pmatrix} \vec{t}_{xx}^{(\delta)} & \vec{t}_{xy}^{(\delta)} & 0 & 0 \\ \vec{t}_{yx}^{(\delta)} & \vec{t}_{yy}^{(\delta)} & 0 & 0 \\ -\vec{r}_{xx}^{(\delta)} & -\vec{r}_{xy}^{(\delta)} & 1 & 0 \\ -\vec{r}_{yx}^{(\delta)} & -\vec{r}_{yy}^{(\delta)} & 0 & 1 \end{pmatrix} \tag{2}$$

where δ (= 1, 2, 3, 4, 5) indicates each layer of metal, respectively. The superscript arrow represents the transmission direction of electromagnetic waves, r and t represent the reflection and transmission coefficient of the monolayer metal, the first subscript indicates the polarization state of the outgoing wave, and the second subscript indicates the incident polarization state. Finally, the upper formula can be simplified as follows:

$$\begin{aligned} E_{\beta x}^{f} &= E_{\alpha x}^{f}\vec{t}_{xx}^{(\delta)} + E_{\alpha y}^{f}\vec{t}_{xy}^{(\delta)} + E_{\beta x}^{b}\overleftarrow{r}_{xx}^{(\delta)} + E_{\beta y}^{b}\overleftarrow{r}_{xy}^{(\delta)} \\ E_{\beta y}^{f} &= E_{\alpha x}^{f}\vec{t}_{yx}^{(\delta)} + E_{\alpha y}^{f}\vec{t}_{yy}^{(\delta)} + E_{\beta x}^{b}\overleftarrow{r}_{yx}^{(\delta)} + E_{\beta y}^{b}\overleftarrow{r}_{yy}^{(\delta)} \\ E_{\alpha x}^{b} &= E_{\beta x}^{b}\overleftarrow{t}_{xx}^{(\delta)} + E_{\beta y}^{b}\overleftarrow{t}_{xy}^{(\delta)} + E_{\alpha x}^{f}\vec{r}_{xx}^{(\delta)} + E_{\alpha y}^{f}\vec{r}_{xy}^{(\delta)} \\ E_{\alpha y}^{b} &= E_{\beta x}^{b}\overleftarrow{t}_{yx}^{(\delta)} + E_{\beta y}^{b}\overleftarrow{t}_{yy}^{(\delta)} + E_{\alpha x}^{f}\vec{r}_{yx}^{(\delta)} + E_{\alpha y}^{f}\vec{r}_{yy}^{(\delta)} \end{aligned} \tag{3}$$

By programming the interference model, the total transmission coefficient of the five-layer structure can be found. The flow chart of the algorithm is shown in Figure 5. T_{yy} is the total transmission coefficient, is the sum of the transmission coefficient of i, i is the iteration times of the interference model, the interference process has countless times, namely the value of i tends to infinity, and the T_{yy} component of each transmission gradually decreases, eventually tends to 0, the greater the value of i, the more accurate the simulation results. We set the value of i to a large enough value (set to 100 in this simulation), so that we can effectively control the error with the theoretical value. Figure 6 shows the calculation results of the proposed interference model compared with the simulation results. Through comparative analysis, we can see that the calculation results of the proposed interference model are basically consistent with the trend of the simulation results. Although there are some errors, it is considered within an acceptable range.

To prove that the proposed cell structure can achieve 360° full phase coverage of the working band, the transmission coefficients and the transmission phase for different structure sizes are analyzed. By changing the opening size and orientation of the two metal rings in the middle, we divided the metasurface cells into eight types, numbered Unit 1 to Unit 8. The structure parameters of the eight cells are shown in Table 1. Figure 7 shows the co-polarized transmission amplitude and transmission phase of the eight cell structures at 0.5-1.3 THz. It can be seen that the transmission efficiency of the eight units is more than 0.7 at 0.7-1.07 THz, and its phase can meet the complete 360° coverage, showing

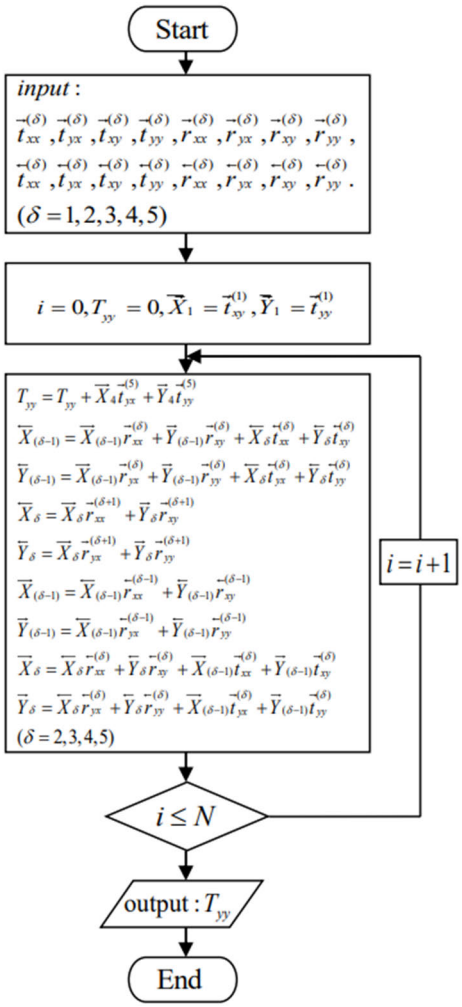

FIGURE 5. Flow chart of the interference model algorithm.

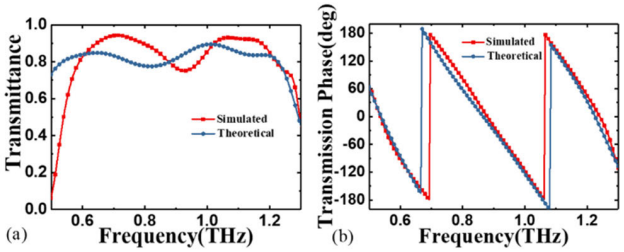

FIGURE 6. Comparison of the co-polarized transmission coefficient between theoretical calculation and simulation (a) transmission amplitude, (b) transmission phase.

good transmission performance. This shows that the proposed metasurface can achieve arbitrary wavefront manipulation within a wideband.

III. MULTIFUNCTIONAL WAVEFRONT CONTROL APPLICATIONS

A. WIDEBAND FOCUS METALENS

Focus metalens plays an important role in the optical system, and it is very valuable to study the high performance

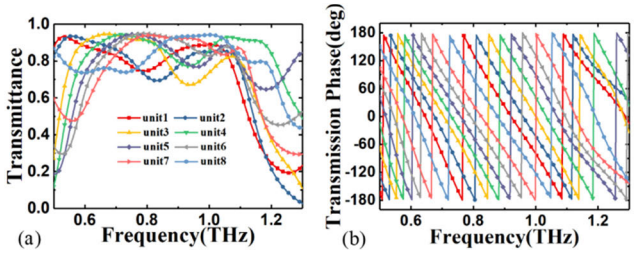

FIGURE 7. (a) Co-polarized transmission amplitude of different cell structures; (b) transmission phase.

TABLE 1. Geometric parameters of the eight cell structures.

	Unit1	Unit2	Unit3	Unit4	Unit5	Unit6	Unit7	Unit8
s	24	43.5	51	15	25	37	52	60
β	45	45	45	-45	-45	-45	-45	-45
θ	45	45	75	30	34	45	45	72

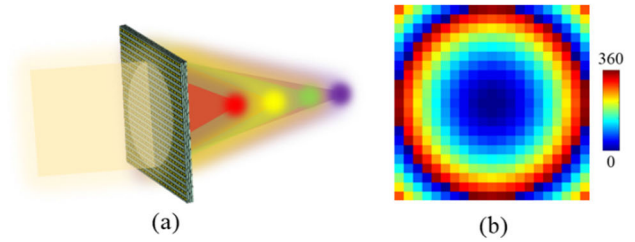

FIGURE 8. (a) Schematic diagram of the focus metalens, and (b) the metalens phase distribution.

and wideband focus metalens. By introducing an appropriate phase gradient on the metasurface, the incident plane wave can be converted into a parabolic wave and converged to the focus, as shown in Figure 8 (a). The phase compensation for each position on the metasurface is [20]:

$$\Phi(x, y) = \frac{2\pi}{\lambda}\left(\sqrt{x^2 + y^2 + f^2} - f\right). \tag{4}$$

where x and y are the coordinates of the metasurface cell structure in the x and y plane, and the central point of the metasurface is (0, 0), and f is the preset focal length. We simulate the focusing effect of the electromagnetic waves in the CST Microwave Studio 2018. In the simulation, the y-polarized plane wave is used as the excitation and propagate along the z direction. Set the open boundary conditions in x, y, z direction to simulate the open vacuum environment. In the simulation, our preset focal length at 1 THz is 1.5 mm. According to the above formula, we can find the compensation phase of each cell structure on the metasurface, as shown in Figure 8 (b).

The metalens designed in this paper consists of 21×21 cells, where each side is guaranteed to have a 360° phase coverage, to ensure a good focus effect. Figure 9 shows the normalized electric field distribution of the xoz-plane at different wavelengths. It can be seen that the

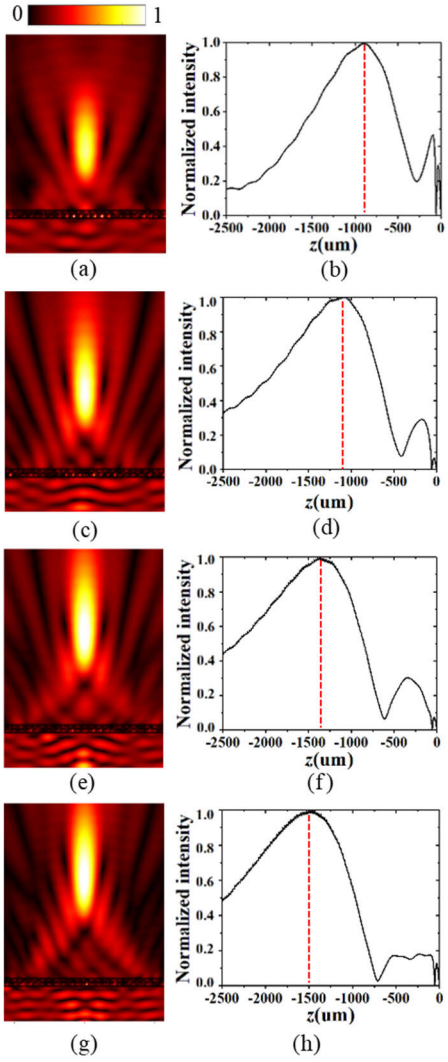

FIGURE 9. E-field distribution at (a) 0.7 THz, (b) 0.8 THz, (c) 0.9 THz, (d)1.0 THz.

metalens can fully focus the incident y-polarization wave, and as the frequency increases, the focal length gradually increases, showing an obvious color difference effect. At the same time, according to Figure 9, when the incident wave is 0.7 THz, the focal length is 890 um; when the incident wave is 0.8 THz, the focal length is 1061 um; when the incident wave is 0.9 THz, the focal length is 1355 um; when the incident wave is 1.0 THz, the focal length is 1479 um. The focal length and wavelength are obviously reverse proportional, according to the formula (4).

The focusing efficiency of the metalens at different wavelengths are calculated. The focusing efficiency is defined as the ratio of the integral of the energy field near the focal point to the total incident energy. The focusing efficiencies of the metalens at the different frequencies mentioned above are 0.61, 0.66, 0.69, and 0.71, respectively. Thus, the proposed broadband metalens exhibits high efficiency over a wide band.

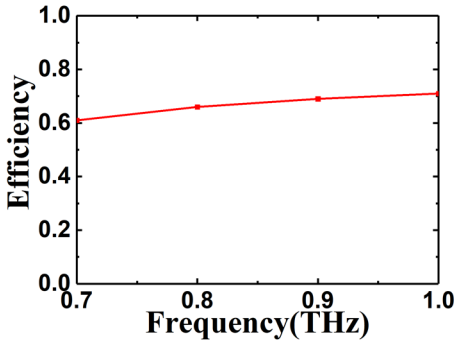

FIGURE 10. Efficiency of the proposed metalens.

B. BROADBAND ORBITAL ANGULAR MOMENTUM GENERATOR

The orbital angular momentum is the orbital part of the angular momentum carried by the electromagnetic wave, which is generated by the energy rotating around the optical axis. The wavefront carrying the orbital angular momentum beam has a vortex shape, so this kind of beam also becomes a vortex beam. Since the eigenstates of the orbital angular momentum carried by vortex beams are orthogonal to each other, different modes can provide independent channel transmission data, thus improving the communication performance. We use the proposed metasurface to design a broadband co-polarized orbital angular momentum.

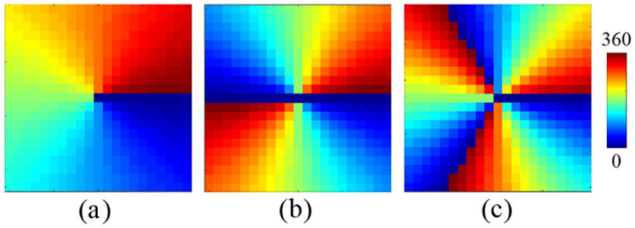

FIGURE 11. Phase distribution of vortex beams (a) $m = +1$ (b) $m = +2$, (c) $m = +3$.

The phase distribution of the vortex beam in the cross section can be expressed as $e^{jm\phi}$, where m and ϕ are the topological charge number and the azimuth angle, respectively. when a compensated phase for the incident wave at specific positions in the metasurface is provided, it can generate a vortex beam carrying the orbital angular momentum. Its phase compensation is expressed by [20]:

$$\varphi_m(x, y) = m \cdot \tan^{-1}\left(\frac{y}{x}\right). \tag{5}$$

where x and y are the coordinates in the metasurface plane, respectively. Here we design the orbital angular momentum generators when the topological charge is equal to $+1$, $+2$, and $+3$, respectively. Figure 11 shows the distribution of phase compensation at $m = +1, +2$, and $+3$. We design three metasurfaces respectively based on these phase compensation distributions, which can produce vortex beams carrying the orbital angular momentum of different orders.

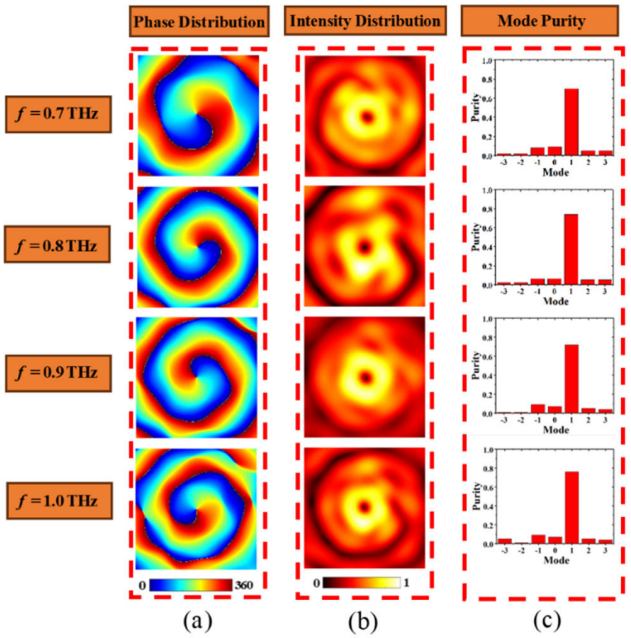

FIGURE 12. (a) y-direction electric field phase of $+1$ order vortex beam at *xoy*-plane at different frequencies; (b) *y*-direction electric field intensity of $+1$ order vortex beam at *xoy*-plane at different frequencies; (c) purity of $+1$ order vortex beam generated at different frequencies.

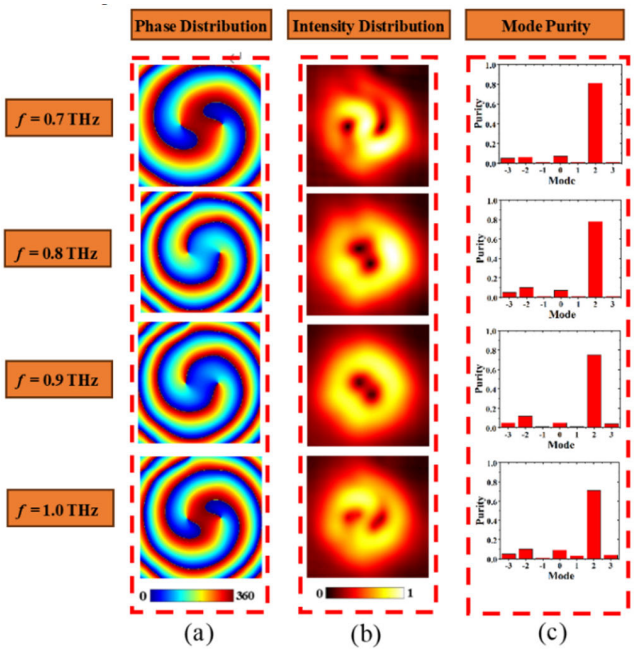

FIGURE 13. (a) *y*-direction electric field phase of $+2$ order vortex beam at *xoy*-plane at different frequencies; (b) *y*-direction electric field intensity of $+2$ order vortex beam at *xoy*-plane at different frequencies; (c) purity of $+2$ order vortex beam generated at different frequencies.

Figure 12 (a) and (b) shows the phase distribution and intensity distribution of the vortex beam generated during the

incidence of the y-polarization wave at different frequencies. It is clear that the phase of the outgoing wave carries a spin arm and rotates clockwise. The electric field intensity shows a "donut" shape, and the central electric field is 0, which is the characteristic singularity of the vortex beam. According to the Fourier transform method, we can find the pattern purity of the vortex beam. Considering the azimuth φ is a periodic function, whose Fourier conjugate is the OAM spectrum, the relationship can be expressed as [27]:

$$\begin{cases} \alpha(\varphi) = \sum_{i=-\infty}^{+\infty} A_m \exp(\mathrm{i}m\varphi) \\ A_m = \frac{1}{2\pi} \int_{-\pi}^{\pi} d\varphi \alpha(\varphi) \exp(-im\varphi) \end{cases} \tag{6}$$

In which $\alpha(\varphi)$ represents the sampling of the phase, and $\exp(\mathrm{i}m\varphi)$ is spiral harmonics. Here, the mode purity of the generated OAM beam is defined as the ratio of the main mode power to the total power of all modes.

Figure 12(c) shows the purity of the vortex beam generated at different frequencies when the main mode is +1. At the incident wave frequency of 0.7 THz, 0.8 THz, 0.9 THz, 1.0 THz, the purity of the orbital angular momentum of +1 is 0.76, 0.77, 0.75 and 0.77 respectively, and at all frequencies, the purity of the secondary modes is almost less than 0.1, showing the high purity performance of the generated vortex beam.

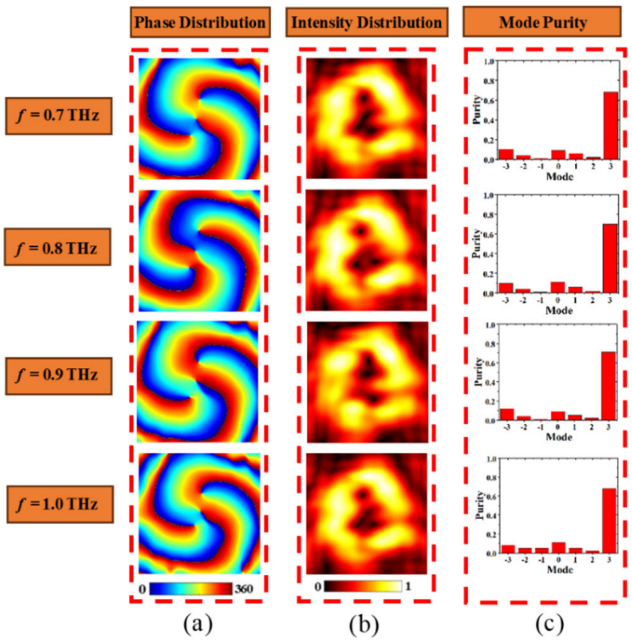

FIGURE 14. (a) y-direction electric field phase of +3 order vortex beam at *xoy*-plane at different frequencies; (b) y-direction electric field intensity of +3 order vortex beam at *xoy*-plane at different frequencies; (c) purity of +3 order vortex beam generated at different frequencies.

Similarly, we simulate the phase, intensity and pattern purity maps generating the vortex beams of the +2 and +3 order, as shown in Figure 13 and Figure 14. As can be seen from Figure 13, the resulting vortex beam has two spin arms, both rotating clockwise, and the electric field intensity also shows a "donut" shape, and has two singularities. When the incidence frequency is 0.7 THz, 0.8 THz, 0.9 THz, 1.0 THz, the purity of the main mode is 0.8, 0.78, 0.77, 0.71, respectively, showing the orbital angular momentum of order +2 with high purity. Figure 14 is the phase, intensity and purity diagram at m = +3. It can be seen that the generated vortex beam has three spin arms, which also rotate clockwise, and the electric field strength has three singularities in the center. At the incident frequency of 0.7 THz, 0.8 THz, 0.9 THz, 1.0 THz, the main mode purity is 0.68, 0.7, 0.71, 0.69, respectively. The above simulation shows that our proposed broadband orbital angular momentum generator can produce high purity OAM in different modes, which also again proves that our proposed metasurface can achieve arbitrary wavefront control over a wide band.

C. BROADBAND THz HOLOGRAPHIC IMAGING

Traditional holographic imaging method is based on the interference between reference light and scattering waves from an object. Digital hologram is a new method that generates a hologram by calculating holographic interference patterns (phase and amplitude information), and then encoding it into the surface structure. Since the metasurface can accurately manipulate the wavefront of electromagnetic waves, holographic imaging based on metasurface is studied recently. In this paper, we use the proposed metasurface to realize the wideband super-holography imaging.

The design of the super-holographic imaging system is divided into two steps: the numerical calculation of the required phase distribution map by using the holographic algorithm, and the phase array construction with the metasurface. In the holographic numerical calculation, the diffraction between the metasurface and the electromagnetic field of the imaging surface is a reversible problem. According to the Rayleigh-Sophie diffraction (Rayleigh Somerfield Diffraction) formula, each unit radiates the electromagnetic field outward, and the unit radiation field can be superimposed on the imaging surface [28]. Assuming the metasurface radiation electric field is:

$$U(x_0, y_0) = \frac{1}{j\lambda} \int\int_s U(x, y) \cos\langle n, r\rangle \frac{\exp(jkr)}{r} dS \tag{7}$$

$U(x_0, y_0)$ and $U(x, y)$ is the electric distributions of the metasurface and the imaging plane.(x_0, y_0) and (x, y) is the position coordinates of the metasurface and the imaging plane.$r = \sqrt{[(x - x_0)^2 + (y - y_0)^2 + zd^2]}$ represents the distance between any two points of the imaging surface and the metasurface, λ is the working wavelength, and zd is the distance between the imaging surface and the metasurface. Since the pure phase holographic method is used in this paper, the amplitude is set to 1 here, and the electric field of the

TABLE 2. Comparison of the metasurface with other works.

References	Metal layers	360° phase coverage band	Polarization type	Coefficient of transmission/ reflection	Application demonstrated
[14]	8	Broadband	CP	T:⩾0.6	OAM
[13]	2	Narrow band	LP	R: ⩾0.9	OAM
[20]	3	Narrow band	LP	T:⩾0.9	OAM
[24]	2	Narrow band	LP	R: ⩾0.99	Metalens
[32]	4	Narrow band	LP	T: ⩾0.86; R: ⩾0.93	Metalens
[33]	3	Narrow band	CP	T: ⩾0.89	OAM
This work	5	Broadband	LP	T: ⩾0.9; R: ⩾0.7	OAM/Metalens/ Holography

imaging surface can be calculated as:

$$U'(x,y) = \frac{1}{j\lambda}\int\int_{s_0} U(x_0,y_0)\cos\langle n,r\rangle \frac{\exp(-jkr^r)}{r} dS_0 \tag{8}$$

We replace $U'(x,y)$ as the amplitude of the image and serve as the input for the calculation. In order to obtain a better imaging quality, the Gerchberg-Saxton (GS) iterative algorithm is used to optimize the phase of the holographic [29]. After several iterations of optimization, the electric field on the hologram is derived, and the amplitude and phase information are extracted. We achieve holographic imaging in transmission mode, based on the proposed metasurface cell structure, by encoding the transmission phase. The designed metasurface holographic plate is composed of 50 × 50 unit structures, and that the letter "H" is taken as the imaging target, as shown in Figure 15 (a). According to the above theoretical description, the metasurface phase distribution is optimized by using the GS algorithm, and the resulting phase distribution is shown in Figure 15 (b). The final metasurface size is 5 mm × 5 mm and the imaging effect is simulated. The *y*-polarization wave is used as the incident source and extract the electric field in the transmission plane at a distance of 1 mm from the metasurface. Figure 15 (c)-(f) shows the normalized electric field distribution at 0.7 THz, 0.8 THz, 0.9 THz and 1.0 THz, respectively. One can be seen that a very clear "H" shape pattern is located in the center of the electric field, indicating that the designed pure phase super-surface holography has good imaging effect.

Table 2 demonstrates the comparison of the proposed metasurface with other works in terms of metal layers, 360° phase coverage band, polarization, coefficient of transmission and reflection. Compared with previous works [13], [14], [15], [16], [17], [18], [19], [20], [21], [22], [23], [24], [25], [26], [27], [28], [29], [30], [31], [32], [33], most of the designs can only achieve a 360° phase coverage at specific frequency points or narrow band. In this paper, the proposed metasurface with efficient co-polarized Terahertz (THz) wave transmission and full 360° phase coverage over a wide band.

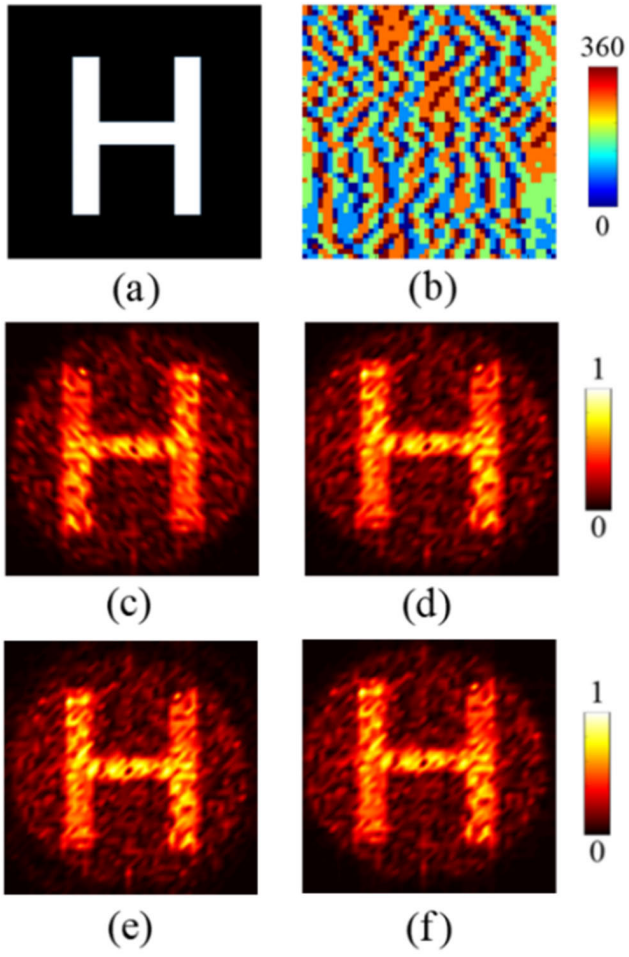

FIGURE 15. (a) Imaging target; (b) phase distribution of the metasurface; (c) electric field distribution at 0.7 THz; (d) electric field distribution at 0.8 THz; (e) electric field distribution at 0.9 THz; (f) electric field distribution at 1.0 THz.

In this paper, we have designed and validated a kind of metasurface by simulation and modeling, and validate its multifunctional properties. Due to our limited experimental conditions, we can not able to further validate our results by experiments. As a matter of face, we can use photolithography, electron-beam metal deposition, and lift-off to fabricate

the metallic structures, and spin coating and thermal curing can be used to apply the polyimide layers [19]. The experiment can done by the following steps: (1) a 4 μm thick polyimide layer is spin coated on a bare GaAs wafer and subsequently cured at 300°C for 150 minutes, to help solidify the liquid polyimide into the thin film. (2) To define the metallic pattern on the polyimide layer by a standard lift-off process, standard photolithographic methods, a deposition of 0.2 μm thick Cu films by electron-beam evaporation, and a lift-off process were used to fabricate the metallic pattern. (3) A 25μm thick polyimide layer was spin coated and thermally cured at 300°C for 150 minutes. (4) The rest of the polyimide layers and metallic patterns were fabricated by repeating the aforementioned steps in sequence. (5) Finally, the GaAs substrate can be mechanically removed by peeling off the polyimide encapsulated structure to establish the free-standing samples.

IV. CONCLUSION

In this paper, we propose a multilayer structure terahertz metasurface with arbitrary copolarized wave phase control on 0.7-1.0 THz broadband and with high trans-mission efficiency. According to the principle of Fabry-Perot resonator, the interference model is established and calculated theoretically, and the co-polarized transmis-sion coefficient of the simulation coincides with the theoretical calculation. Based on this, we designed a metalens with a wide band, which can realize the focus effect on 0.7-1.0 THz, and reflect the obvious color difference effect. Then, we implement an orbital angular momentum generator with a broad band, generating vortex beams of multiple modes exhibiting high pattern purity. Finally, we achieved holographic imaging, which shows good imaging effect at 0.7-1.0 THz. The proposed metasurface will provide new ideas for the design of broadband multi-functional devices, which is expected to achieve engineering applications in the subsequent THz communication field.

REFERENCES

[1] B. B. Hu and M. C. Nuss, "Imaging with terahertz waves," *Opt. Lett.*, vol. 20, no. 16, pp. 1716–1718, 1995.

[2] B. Scherger, N. Born, C. Jansen, S. Schumann, M. Koch, and K. Wiesauer, "Compression molded terahertz transmission blaze-grating," *IEEE Trans. THz Sci. Technol.*, vol. 2, no. 5, pp. 556–561, Sep. 2012.

[3] T. Kleine-Ostmann, K. Pierz, G. Hein, P. Dawson, and M. Koch, "Audio signal transmission over THz communication channel using semiconductor modulator," *Electron. Lett.*, vol. 40, no. 2, pp. 124–126, 2004.

[4] B. Reinhard, O. Paul, and M. Rahm, "Metamaterial-based photonic devices for terahertz technology," *IEEE J. Sel. Topics Quantum Electron.*, vol. 19, no. 1, Jan. 2013, Art. no. 8500912.

[5] S. Zhang, W. Fan, K. J. Malloy, S. R. J. Brueck, N. C. Panoiu, and R. M. Osgood, "Near-infrared double negative metamaterials," *Opt. Exp.*, vol. 13, no. 13, p. 4922, 2005.

[6] E. Plum, J. Zhou, J. Dong, V. A. Fedotov, T. Koschny, C. M. Soukoulis, and N. I. Zheludev, "Metamaterial with negative index due to chirality," *Phys. Rev. B, Condens. Matter*, vol. 79, no. 3, Jan. 2009, Art. no. 035407.

[7] C. L. Holloway, E. F. Kuester, J. A. Gordon, J. O'Hara, J. Booth, and D. R. Smith, "An overview of the theory and applications of metasurfaces: The two-dimensional equivalents of metamaterials," *IEEE Antennas Propag. Mag.*, vol. 54, no. 2, pp. 10–35, Apr. 2012.

[8] J. Valentine, S. Zhang, T. Zentgraf, E. Ulin-Avila, D. A. Genov, G. Bartal, and X. Zhang, "Three-dimensional optical metamaterial with a negative refractive index," *Nature*, vol. 455, no. 7211, pp. 376–379, Sep. 2008.

[9] X. Zang, H. Ding, Y. Intaravanne, L. Chen, Y. Peng, J. Xie, Q. Ke, A. V. Balakin, A. P. Shkurinov, X. Chen, Y. Zhu, and S. Zhuang, "A multi-foci metalens with polarization-rotated focal points," *Laser Photon. Rev.*, vol. 13, no. 12, Dec. 2019, Art. no. 1900182.

[10] X. Li, S. Xiao, B. Cai, Q. He, T. J. Cui, and L. Zhou, "Flat metasurfaces to focus electromagnetic waves in reflection geometry," *Opt. Lett.*, vol. 37, no. 23, pp. 4940–4942, 2012.

[11] X. Liu, K. Fan, I. V. Shadrivov, and W. J. Padilla, "Experimental realization of a terahertz all-dielectric metasurface absorber," *Opt. Exp.*, vol. 25, no. 1, pp. 191–201, 2017.

[12] X. Chen, L. Huang, H. Mühlenbernd, G. Li, B. Bai, Q. Tan, G. Jin, C.-W. Qiu, S. Zhang, and T. Zentgraf, "Dual-polarity plasmonic metalens for visible light," *Nature Commun.*, vol. 3, no. 1, p. 1198, Nov. 2012.

[13] F. Bi, Z. Ba, and X. Wang, "Metasurface-based broadband orbital angular momentum generator in millimeter wave region," *Opt. Exp.*, vol. 26, no. 20, p. 25693, 2018.

[14] S. Jiang, C. Chen, H. Zhang, and W. Chen, "Achromatic electromagnetic metasurface for generating a vortex wave with orbital angular momentum (OAM)," *Opt. Exp.*, vol. 26, no. 5, p. 6466, 2018.

[15] H. Wang, S. Yu, N. Kou, Z. Ding, and Z. Zhang, "Cylindrical holographic impedance metasurface for OAM vortex wave generation," *Appl. Phys. Lett.*, vol. 120, no. 14, Apr. 2022, Art. no. 143504.

[16] W. Zhu, F. Xiao, M. Kang, and M. Premaratne, "Coherent perfect absorption in an all-dielectric metasurface," *Appl. Phys. Lett.*, vol. 108, no. 12, Mar. 2016, Art. no. 121901.

[17] Z. Ding, W. Su, H. Lu, H. Wu, and H. Yao, "Terahertz absorber based on double-layer graphene metasurface with tunable absorption window and intensity," *Opt. Laser Technol.*, vol. 163, Aug. 2023, Art. no. 109446, doi: 10.1016/j.optlastec.2023.109446.

[18] T. Badloe, J. Mun, and J. Rho, "Metasurfaces-based absorption and reflection control: Perfect absorbers and reflectors," *J. Nanomaterials*, vol. 2017, Jan. 2017, Art. no. 2361042.

[19] N. K. Grady, J. E. Heyes, D. R. Chowdhury, Y. Zeng, M. T. Reiten, A. K. Azad, A. J. Taylor, D. A. R. Dalvit, and H.-T. Chen, "Terahertz metamaterials for linear polarization conversion and anomalous refraction," *Science*, vol. 340, no. 6138, pp. 1304–1307, Jun. 2013.

[20] J. Fan and Y. Cheng, "Broadband high-efficiency cross-polarization conversion and multi-functional wavefront manipulation based on chiral structure metasurface for terahertz wave," *J. Phys. D, Appl. Phys.*, vol. 53, no. 2, Jan. 2020, Art. no. 025109.

[21] L. Liu, X. Zhang, M. Kenney, X. Su, N. Xu, C. Ouyang, Y. Shi, J. Han, W. Zhang, and S. Zhang, "Broadband metasurfaces with simultaneous control of phase and amplitude," *Adv. Mater.*, vol. 26, no. 29, pp. 5031–5036, Aug. 2014.

[22] B. He, J. Fan, Y. Cheng, F. Chen, H. Luo, and R. Gong, "Thermally tunable terahertz vortex beam generator based on an InSb metasurface," *J. Opt. Soc. Amer. B, Opt. Phys.*, vol. 38, no. 5, pp. 1518–1524, 2021.

[23] H. Zhao, B. Quan, X. Wang, C. Gu, J. Li, and Y. Zhang, "Demonstration of orbital angular momentum multiplexing and demultiplexing based on a metasurface in the terahertz band," *ACS Photon.*, vol. 5, no. 5, pp. 1726–1732, 2017.

[24] J. Zhang, L. Yang, L. Li, T. Zhang, H. Li, Q. Wang, Y. Hao, M. Lei, and K. Bi, "High-efficiency polarization conversion phase gradient metasurface for wideband anomalous reflection," *J. Appl. Phys.*, vol. 122, no. 1, Jul. 2017, Art. no. 014501.

[25] Y. Liu, C. Liu, K. Song, M. Li, and X. Zhao, "A broadband high-transmission gradient phase discontinuity metasurface," *J. Phys. D, Appl. Phys.*, vol. 51, no. 9, Mar. 2018, Art. no. 095103.

[26] H. Yang, Z. Xie, Z. Zhou, and X. Yuan, "Full-space polarization-regulated lightwave steering via single-layer metasurfaces," *J. Phys. D, Appl. Phys.*, vol. 54, no. 1, Jan. 2021, Art. no. 015102, doi: 10.1088/1361-6463/abb7b8.

[27] M. J. Strain, X. Cai, J. Wang, J. Zhu, D. B. Phillips, L. Chen, M. Lopez-Garcia, J. L. O'Brien, M. G. Thompson, M. Sorel, and S. Yu, "Fast electrical switching of orbital angular momentum modes using ultra-compact integrated vortex emitters," *Nature Commun.*, vol. 5, no. 1, p. 4856, Sep. 2014.

[28] Z. Zhu, Y. Cheng, Y. Li, J. Wang, and S. Qu, "Four-function metasurface based on a tri-band integrated meta-atom for full space control of circularly polarized waves," *Opt. Exp.*, vol. 29, no. 26, pp. 42569–42579, 2021.

[29] Q. Wang, E. Plum, Q. Yang, X. Zhang, Q. Xu, Y. Xu, J. Han, and W. Zhang, "Reflective chiral meta-holography: Multiplexing holograms for circularly polarized waves," *Light, Sci. Appl.*, vol. 7, no. 1, Jun. 2018.
[30] C. Wu, S. Kumar, Y. Kan, D. Komisar, Z. Wang, S. I. Bozhevolnyi, and F. Ding, "Room-temperature on-chip orbital angular momentum single-photon sources," *Sci. Adv.*, vol. 8, no. 2, Jan. 2022, Art. no. eabk3075.
[31] S. Tang, X. Li, W. Pan, J. Zhou, T. Jiang, and F. Ding, "High-efficiency broadband vortex beam generator based on transmissive metasurface," *Opt. Exp.*, vol. 27, no. 4, p. 4281, Feb. 2019.
[32] T. Cai, G. Wang, S. Tang, H. Xu, J. Duan, H. Guo, F. Guan, S. Sun, Q. He, and L. Zhou, "High-efficiency and full-space manipulation of electromagnetic wave fronts with metasurfaces," *Phys. Rev. Appl.*, vol. 8, no. 3, Sep. 2017, Art. no. 034033.
[33] X. Jing, Y. Ke, Y. Tian, H. Gan, Y. He, C. Li, and Z. Hong, "Manipulation of terahertz wave based on three-layer transmissive Pancharatnam–Berry phase metasurface," *IEEE Access*, vol. 8, pp. 164795–164806, 2020.

SU ZONG received the B.E. degree in information and computing sciences from Jiangxi University of Science and Technology (JXUST), Ganzhou, China, in 2006, and the M.E. degree in computer technology from Nanchang University (NCU), Nanchang, China, in 2011. His current research interests include electromagnetic calculation and communication theory.

JIAJUN LIANG (Senior Member, IEEE) received the B.E. degree in electronic science and technique from Guilin University of Electronic Technology (GUET), Guilin, China, in 2012, the M.E. degree in radio physics from the University of Electronic Science and Technology of China (UESTC), Chengdu, China, in 2015, and the Ph.D. degree in information and communication engineering from Shenzhen University, Shenzhen, China, in 2018. He was with the Department of the Physics, The Hong Kong University of Science and Technology, as a Research Assistant, from November 2016 to November 2017. He is currently with the School of Physics and Telecommunication Engineering, Yulin Normal University. His current research interests include metasurface, microwave, and millimetre wave antenna.